# NUMERICAL SIMULATION OF SEISMIC ATTENUATION DUE TO WAVE-INDUCED FLUID FLOW

## Juan E. Santos[a,b], J. Germán Rubino[b] and José M. Carcione[c]

[a]*CONICET, Departamento de Geofísica Aplicada, Facultad de Ciencias Astronómicas y Geofísicas, Universidad Nacional de La Plata, Paseo del Bosque S/N, La Plata (1900) Argentina and Department of Mathematics, Purdue University, 150 N. University Street, West Lafayette, Indiana, 47907-2067, USA, santos@fcaglp.fcaglp.unlp.edu.ar ,*

[b]*CONICET, Departamento de Geofísica Aplicada, Facultad de Ciencias Astronómicas y Geofísicas, Universidad Nacional de La Plata, Paseo del Bosque S/N, La Plata (1900) Argentina, grubino@fcaglp.fcaglp.unlp.edu.ar,*

[c]*Istituto Nazionale di Oceanografia e di Geofisica Sperimentale (OGS), Borgo Grotta Gigante 42c, 34010 Sgonico, Trieste, Italy,, jcarcione@ogs.trieste.it*

**Keywords:** Seismic Attenuation, Finite Elements, Parallel Algorithms

**Abstract.** Seismic data from sedimentary rocks usually exhibits attenuation levels than can not be explained by existing theoretical models. An important dissipation mechanism for waves in heterogeneous poroelastic media is the effect of wave-induced fluid flow created by mesoscopic scale heterogeneities, known as mesoscopic loss. Mesoscopic length scales are those larger than pore size but smaller than wavelengths in the seismic range (1- 100 Hz). A typical mesoscopic heterogeneity has a size of tens of centimeters. Mesoscopic heterogeneities can be due to local variations in lithological properties or to patches of immiscible fluids. For example, a fast compressional wave traveling across a porous rock saturated with water and patches of gas induces a greater fluid pressure in the gas patches than in the water saturated parts of the material. This in turn generates fluid flow and slow Biot waves which diffuse away from the gas-water interfaces generating significant losses in the seismic range. In this work an iterative domain decomposition finite element procedure is presented and employed to solve Biot's equations of motion for saturated poroelastic materials. The domain decomposition procedure is naturally parallelizable, which is a necessity in this type of simulations due to the large number of degrees of freedom needed to accurately represent these attenuation effects. The numerical simulations, run on a parallel computer, were designed to show the effects of the wave-induced fluid flow on the traveling waves in the seismic range of frequencies. The simulated recorded traces show evidence of the mesoscopic loss mechanism in this type of materials.

## 1 INTRODUCTION

The propagation of waves in a porous elastic solid saturated by a single–phase compressible viscous fluid was first analyzed by Biot in several classic papers (Biot, 1956a), (Biot, 1956b). Biot assumed that the fluid may flow relative to the solid frame causing friction. Biot also predicted the existence of two compressional waves, denoted here as P1 and P2 compressional waves, and one shear or S wave. The three waves suffer attenuation and dispersion effects in the seismic to the ultrasonic range of frequencies. The P1 and shear waves have a behavior similar to that in an elastic solid, with high phase velocities, low attenuation and very little dispersion. The P2 wave behaves as a diffusion–type wave due to its low phase velocity and very high attenuation and dispersion. One important cause of attenuation at seismic frequencies in fluid-saturated porous media is wave-induced flow at mesoscopic scale heterogeneities, which are small compared with the wavelength but larger than the average pore size. As pointed out by White, (White et al., 1975), sometimes gas saturation over a large vertical section occurs in thin layers, separated by liquid-saturated layers. This is the simplest case of mesoscopic heterogeneities and White showed that in this case fluid-flow effects add up and play a major role. Numerical simulations to analyze attenuation effects in an homogeneous sandstone saturated with brine and spherical gas pockets at laboratory frequencies were presented in (Carcione et al., 2003) and (Helle et al., 2003).

In this article we describe the use of a parallel iterative finite element domain decomposition procedure to simulate the propagation of waves in laminated porous media in the seismic range of frequencies. The algorithm employs the nonconforming rectangular element defined in (J. Douglas Jr. et al., 1999) to approximate the displacement vector in the solid phase. The dispersion analysis presented in (Zyserman et al., 2003) shows that using this nonconforming element allows for a reduction in the number of points per wavelength necessary to reach a desired accuracy. It is also the case that the use of nonconforming elements reduces the amount of information that needs to be exchanged in any parallel implementation of the algorithm, as compared with the corresponding procedure using conforming elements of the same order. The displacement in the fluid phase is approximated using the vector part of the Raviart-Thomas-Nedelec mixed finite element space of zero order, which is a conforming space (Raviart and Thomas, 1975; Nedelec, 1980). The convergence analysis of this type of iterative algorithm is presented in (Santos and Sheen, 2006). The numerical experiments were run in the IBM SP2 and the Community Cluster parallel computers at Purdue University under the MPI standards. The synthetic traces show clearly the mesoscopic loss mechanism due to the wave-induced flow, and the observed attenuation is in very good agreement with that predicted by the White theory.

## 2 REVIEW OF BIOT THEORY

We consider a porous solid saturated by a single phase, compressible viscous fluid and assume that the whole aggregate is isotropic. Let $u^s = (u_i^s)$ and $\tilde{u}^f = (\tilde{u}_i^f)$, $i = 1, \cdots, d$ denote the averaged displacement vectors of the solid and fluid phases, respectively, where $d$ denotes the Euclidean dimension. Also let

$$u^f = \phi(\tilde{u}^f - u^s),$$

be the average relative fluid displacement per unit volume of bulk material, where $\phi$ denotes the effective porosity. Also set $u = (u^s, u^f)$ and note that

$$\xi = -\nabla \cdot u^f,$$

represents the change in fluid content.

Let $\varepsilon_{ij}(u^s)$ be the strain tensor of the solid. Also, let $\sigma_{ij}$, $i, j = 1, \cdots, d$, and $p_f$ denote the stress tensor of the bulk material and the fluid pressure, respectively. Following ( Biot, 1962), the stress-strain relations can be written in the form:

$$\sigma_{ij}(u) = 2\mu\,\varepsilon_{ij}(u^s) + \delta_{ij}(\lambda_c\,\nabla \cdot u^s - \alpha\,K_{av}\,\xi), \tag{1a}$$

$$p_f(u) = -\alpha\,K_{av}\,\nabla \cdot u^s + K_{av}\xi. \tag{1b}$$

The coefficient $\mu$ is equal to the shear modulus of the bulk material, considered to be equal to the shear modulus of the dry matrix. Also

$$\lambda_c = K_c - \frac{2}{d}\mu,$$

with $K_c$ being the bulk modulus of the saturated material. Following (Santos et al., 1992; Gassmann, 1951) the coefficients in (1) can be obtained from the relations

$$\alpha = 1 - \frac{K_m}{K_s}, \quad K_{av} = \left(\frac{\alpha - \phi}{K_s} + \frac{\phi}{K_f}\right)^{-1} \quad K_c = K_m + \alpha^2 K_{av},$$

where $K_s$, $K_m$ and $K_f$ denote the bulk modulus of the solid grains composing the solid matrix, the dry matrix and the the saturant fluid, respectively. The coefficient $\alpha$ is known as the effective stress coefficient of the bulk material.

## 2.1 The equations of motion

Let us consider an open bounded domain $\Omega \subset R^d$ of bulk material with boundary $\Gamma = \partial\Omega$. Let $\rho_s$ and $\rho_f$ denote the mass densities of the solid grains and the fluid and let

$$\rho_b = (1 - \phi)\rho_s + \phi\rho_f$$

denote the mass density of the bulk material. Let the positive definite matrix $\mathcal{P}$ and the nonnegative matrix $\mathcal{B}$ be defined by

$$\mathcal{P} = \begin{pmatrix} \rho_b I & \rho_f I \\ \rho_f I & g I \end{pmatrix}, \quad \mathcal{B} = \begin{pmatrix} 0I & 0I \\ 0I & bI \end{pmatrix}.$$

Here $I$ denoted the identity matrix in $R^{d \times d}$. Also, the mass coupling coefficient $g$ represents the inertial effects associated with dynamic interactions between the solid and fluid phases, while the coefficient $b$ includes the viscous coupling effects between such phases. They are given by the relations

$$b = \frac{\eta}{k}, \qquad g = \frac{S\rho_f}{\phi}, \qquad S = \frac{1}{2}\left(1 + \frac{1}{\phi}\right), \tag{2}$$

where $\eta$ is the fluid viscosity and $k$ the absolute permeability. $S$ is known as the structure or tortuosity factor.

Next, let $\mathcal{L}(u)$ be the second order differential operator defined by

$$\mathcal{L}(u) = (\nabla \cdot \sigma(u), -\nabla p_f(u))^t.$$

Then if $\omega = 2\pi f$ is the angular frequency and $F(x,\omega) = (F^s(x,\omega), F^f(x,\omega))$ is the external source, the equations of motion, stated in the space-frequency domain are (Biot, 1956a,b),

$$-\omega^2 \mathcal{P} u(x,\omega) + i\omega \mathcal{B} u(x,\omega) - \mathcal{L}(u(x,\omega)) = F(x,\omega), \quad x \in \Omega. \tag{3}$$

It was shown by Biot (Biot, 1956a,b) that in this type of media two compressional waves, denoted here as P1 and P2, and one shear or S wave can propagate. The P1 and S waves correspond to the classical compressional and shear waves propagating in elastic or viscoelastic isotropic solids. The additional P2 slow mode is a wave strongly attenuated in the low frequency range, associated with the motion out of phase of the solid and fluid phases.

In order to state a boundary condition needed to completely define our differential model we need to introduce some notation. Let us denote by $\nu$ the unit outer normal on $\Gamma$. In the 2D case let $\chi$ be a unit tangent on $\Gamma$ so that $\{\nu, \chi\}$ is an orthonormal system on $\Gamma$. In the 3D case let $\chi^1$ and $\chi^2$ be two unit tangents on $\Gamma$ so that $\{\nu, \chi^1, \chi^2\}$ is an orthonormal system on $\Gamma$. Then, in the 2D case set

$$\mathcal{G}_\Gamma(u) = \left( \sigma(u)\nu \cdot \nu, \sigma(u)\nu \cdot \chi, p_f(u) \right)^t, \quad S_\Gamma(u) = \left( u^s \cdot \nu, u^s \cdot \chi, u^f \cdot \nu \right)^t, \tag{4}$$

and in the 3D case set

$$\begin{aligned}
\mathcal{G}_\Gamma(u) &= \left( \sigma(u)\nu \cdot \nu, \sigma(u)\nu \cdot \chi^1, \sigma(u)\nu \cdot \chi^2, p_f(u) \right)^t, \\
S_\Gamma(u) &= \left( u^s \cdot \nu, u^s \cdot \chi^1, u^s \cdot \chi^2, u^f \cdot \nu \right)^t.
\end{aligned} \tag{5}$$

Let us consider the solution of (3) with the following absorbing boundary condition

$$-\mathcal{G}_\Gamma(u(x,\omega)) = i\omega \mathcal{D} S_\Gamma(u(x,\omega)), \qquad x \in \Gamma. \tag{6}$$

The matrix $\mathcal{D}$ in (6) is positive definite. In the 2D case it is given by the following relations, with the obvious extension to the 3D case: $\mathcal{D} = \mathcal{A}^{\frac{1}{2}} \mathcal{N}^{\frac{1}{2}} \mathcal{A}^{\frac{1}{2}}$, where $\mathcal{N} = \mathcal{A}^{-\frac{1}{2}} \mathcal{M}^{\frac{1}{2}} \mathcal{A}^{-\frac{1}{2}}$ and

$$\mathcal{A} = \begin{pmatrix} \rho_b & 0 & \rho_f \\ 0 & \rho_b - \dfrac{(\rho_f)^2}{g} & 0 \\ \rho_f & 0 & g \end{pmatrix}, \quad \mathcal{M} = \begin{pmatrix} \lambda_c + 2\mu & 0 & \alpha\, K_{av} \\ 0 & \mu & 0 \\ \alpha\, K_{av} & 0 & K_{av} \end{pmatrix}. \tag{7}$$

To perform the numerical simulations needed to represent the mesoscopic loss mechanism, the approximate solution of (3) with the boundary condition (6) would require the solution of a huge linear system of equations due to the large number of degrees of freedom needed to properly discretize the physical model. Since the associated algebraic problem is complex valued and noncoercive, no known efficient iterative global solvers can be employed. To tackle this difficulty, in the next section a parallel iterative domain decomposition algorithm is presented.

## 3   THE ITERATIVE DOMAIN DECOMPOSITION ALGORITHM

We consider the solution of (3) in a rectangular poroelastic domain $\Omega$ in the $(x,y)$–plane using a parallelizable iterative domain decomposition procedure. Let $\mathcal{T}^h$ be a non-overlapping partition of $\Omega$ into rectangles $\Omega_j$ of diameter bounded by $h$ such that $\overline{\Omega} = \cup_{j=1}^J \overline{\Omega}_j$. Set $\Gamma_j =$

$\partial\Omega \cap \partial\Omega_j$, $\Gamma_{jk} = \partial\Omega_j \cap \partial\Omega_k$, and denote by $\xi_j$ and $\xi_{jk}$ the midpoints of $\Gamma_j$ and $\Gamma_{jk}$, respectively. Let us denote by $\nu_{jk}$ the unit outer normal on $\Gamma_{jk}$ from $\Omega_j$ to $\Omega_k$ and by $\nu_j$ the unit outer normal to $\Gamma_j$. Let $\chi_j$ and $\chi_{jk}$ be two unit tangents on $\Gamma_j$ and $\Gamma_{jk}$ so that $\{\nu_j, \chi_j\}$ and $\{\nu_{jk}, \chi_{jk}\}$ are orthonormal systems on $\Gamma_j$ and $\Gamma_{jk}$, respectively.

Consider the decomposition of problem (3) and (6) over $\Omega_j$ as follows: for $j = 1, \ldots, J$, find $u_j(x, \omega)$ satisfying

$$-\omega^2 \mathcal{P} u_j + i\omega \mathcal{B} u_j - \mathcal{L}(u_j) = F, \quad \Omega_j, \tag{8a}$$

$$\mathcal{G}_{\Gamma_{jk}}(u_j) + i\omega\beta_{jk} S_{\Gamma_{jk}}(u_j) = \mathcal{G}_{\Gamma_{kj}}(u_k) - i\omega\beta_{jk} S_{\Gamma_{kj}}(u_k), \qquad \Gamma_{jk}, \tag{8b}$$

$$-\mathcal{G}_{\Gamma_j}(u_j) = i\omega\mathcal{D} S_{\Gamma_j}(u_j), \qquad \Gamma_j, \tag{8c}$$

where $\mathcal{G}_{\Gamma_{jk}}$ and $\mathcal{G}_{\Gamma_j}$ are defined as in (4). Here $\beta_{jk}$ is a positive definite matrix function defined on the interior boundaries $\Gamma_{jk}$. The Robin transmission conditions (8b) impose the continuity of the solid displacement, the normal component of the fluid displacement and the stresses at the interior interfaces $\Gamma_{jk}$.

The spatial discretization is performed as follows. To approximate each component of the solid displacement vector we employ the nonconforming finite element space as in (J. Douglas Jr. et al., 1999), while to approximate the fluid displacement vector we choose the vector part of the Raviart-Thomas-Nedelec space (Raviart and Thomas, 1975; Nedelec, 1980) of zero order. More specifically, let us define the finite element space locally on a reference square $\widehat{R} = [-1, 1]^2$ as follows. For each component of the solid displacement, set

$$\widehat{\mathcal{NC}}(\widehat{R}) = \text{Span}\{1, \hat{x}, \hat{y}, \alpha(\hat{x}) - \alpha(\hat{y})\}, \quad \alpha(\hat{x}) = \hat{x}^2 - \frac{5}{3}\hat{x}^4,$$

with the degrees of freedom being the values at the midpoint of each edge of $\widehat{R}$. Next, for the fluid displacement vector, if $\psi^L(\hat{x}) = \dfrac{-1 + \hat{x}}{2}$, $\psi^R(\hat{x}) = \dfrac{1 + \hat{x}}{2}$, $\psi^B(\hat{y}) = \dfrac{-1 + \hat{y}}{2}$, $\psi^T(\hat{y}) = \dfrac{1 + \hat{y}}{2}$, we define

$$\widehat{\mathcal{W}}(\widehat{R}) = \text{Span}\big\{(\psi^L(\hat{x}), 0)^t, (\psi^R(\hat{x}), 0)^t, (0, \psi^B(\hat{y}))^t, (0, \psi^T(\hat{y}))^t\big\}.$$

Figure 1 shows the local degrees of freedom (dofs) associated with each component of the solid displacement and the fluid displacement vector.

Now we define the finite element spaces associated with the partition $\mathcal{T}^h$ by scaling and translations in the usual fashion as follows. For each $\Omega_j$, let $F_{\Omega_j} : \widehat{R} \to \Omega_j$ be an invertible affine mapping such that $F_{\Omega_j}(\widehat{R}) = \Omega_j$, and define

$$\mathcal{NC}_j^h = \{v = (v_1, v_2)^t : v_i = \hat{v}_i \circ F_{\Omega_j}^{-1}, \hat{v}_i \in \widehat{\mathcal{NC}}(\widehat{R}), \; i = 1, 2\},$$

$$\mathcal{W}_j^h = \{w : w = \hat{w} \circ F_{\Omega_j}^{-1}, \hat{w} \in \widehat{\mathcal{W}}(\widehat{R})\}.$$

Setting

$$\mathcal{NC}^h = \{v : v_j = v|_{\Omega_j} \in \mathcal{NC}_j^h, \; v_j(\xi_{jk}) = v_k(\xi_{jk}) \; \forall (j, k)\},$$

$$\mathcal{W}^h = \{w \in H(\text{div}; \Omega) : w_j = w|_{\Omega_j} \in \mathcal{W}_j^h\},$$

the global finite element space to approximate the solution $u$ of (3) and (6) is defined by

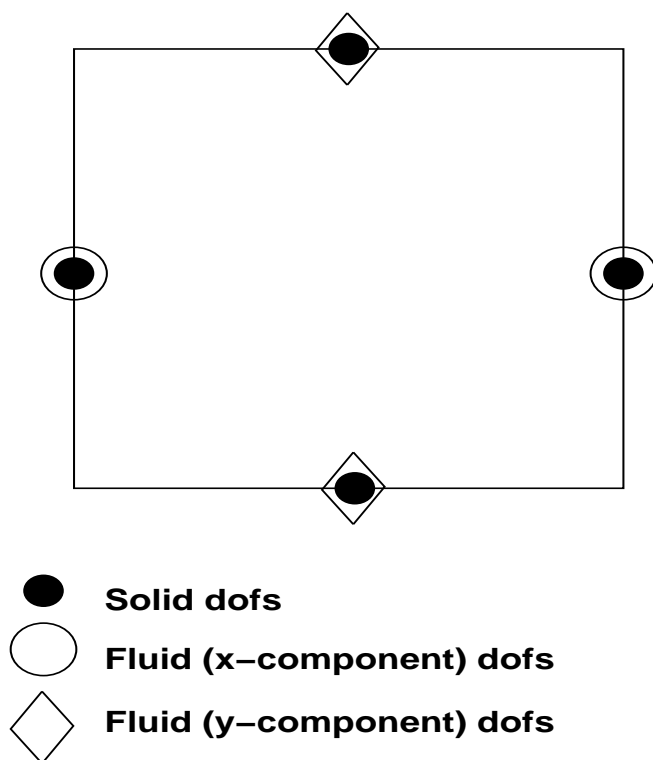$$\mathcal{V}^h = \mathcal{NC}^h \times \mathcal{W}^h.$$

Figure 1: Local degrees of freedom (dofs) associated with each component of the solid displacement and the fluid displacement vector.

Standard approximation theory implies that, for all $\varphi = \left(\varphi^{(1)}, \varphi^{(2)}\right)^t \in [H^2(\Omega)]^2 \times H^1(\mathrm{div}; \Omega)$,

$$\inf_{p \in \mathcal{N}C^h} \left[ \|\varphi^{(1)} - p\|_0 + h \left( \sum_j \|\varphi^{(1)} - p\|_{1,Q_j}^2 \right)^{\frac{1}{2}} \right] \leq Ch^2 \|\varphi^{(1)}\|_2, \tag{9a}$$

$$\inf_{p \in \mathcal{W}^h} \|\varphi^{(2)} - p\|_0 \leq Ch \|\varphi^{(2)}\|_1, \tag{9b}$$

$$\inf_{p \in \mathcal{W}^h} \|\varphi^{(2)} - p\|_{H(\mathrm{div};\Omega)} \leq Ch \left( \|\varphi^{(2)}\|_1 + \|\nabla \cdot \varphi^{(2)}\|_1 \right). \tag{9c}$$

Next, following (J. Douglas Jr. et al., 1999; Santos and Sheen, 2006), we introduce a set of Lagrange multipliers $\lambda_{jk}^h$ associated with the values of the forces at the mid points $\xi_{jk}$ of $\Gamma_{jk}$ in the sense that $\lambda_{jk}^h \sim \mathcal{G}_{jk}(u_j)(\xi_{jk})$. The Lagrange multipliers $\lambda_{jk}^h$ belong to the following space of functions defined on the interior interfaces $\Gamma_{jk}$:

$$\Lambda^h = \left\{ \lambda^h \colon \lambda^h|_{\Gamma_{jk}} = \lambda_{jk}^h \in [P_0(\Gamma_{jk})]^3 = \Lambda_{jk}^h, \, \forall \{j,k\} \right\},$$

where $P_0(\Gamma_{jk})$ denotes the constant functions on $\Gamma_{jk}$.

Next, we state a domain decomposition iteration using a variational formulation. Let us denote by $(\cdot, \cdot)_j$ the usual complex inner product in $L^2(\Omega_j)$. Moreover, for $\Gamma = \Gamma_j$ or $\Gamma = \Gamma_{jk}$ let $\langle \cdot, \cdot \rangle_\Gamma$ denote the complex inner product in $L^2(\Gamma)$, and let $\langle\langle u, v \rangle\rangle_\Gamma$ denote its approximation by the mid–point quadrature: $\langle\langle u, v \rangle\rangle_\Gamma = (u\overline{v})(\xi_{jk})|\Gamma|$ where $|\Gamma|$ is the measure of $\Gamma$.

The domain decomposition iteration is defined as follows: For all $j = 1, \cdots, J$, choose an initial guess $\left( u_j^{\{h,0\}}, \lambda_{jk}^{\{h,0\}} \right) \in \mathcal{N}C_j^h \times \mathcal{W}_j^h \times \Lambda_{jk}^h$. Then, for $n = 1, 2, 3, \cdots$, compute

$\left(u_j^{\{h,n\}}, \lambda_{jk}^{\{h,n\}}\right) \in \mathcal{N}C_j^h \times \mathcal{W}_j^h \times \Lambda_{jk}^h$ as the solution of the equations

$$-\omega^2 \left(\mathcal{P}u_j^{\{h,n\}}, v\right)_j + i\omega \left(\mathcal{B}u_j^{\{h,n\}}, v\right)_j \tag{10a}$$

$$+ \sum_{l,m} \left(\sigma_{lm}(u_j^{\{h,n\}}), \varepsilon_{lm}(v^{(1)})\right)_j - \left(p_f(u_j^{\{h,n\}}), \nabla \cdot v^{(2)})\right)_j$$

$$+ i\omega \left\langle \mathcal{D}\, S_{\Gamma_j}(u_j^{\{h,n\}}), S_{\Gamma_j}(v)\right\rangle_{\Gamma_j} + \sum_k \left\langle i\omega\beta_{jk}\mathcal{S}_{\Gamma_{jk}}(u_j^{\{h,n\}}), \mathcal{S}_{\Gamma_{jk}}(v)\right\rangle_{\Gamma_{jk}}$$

$$= (F, v)_{\Omega_j} - \sum_k \left\langle i\omega\beta_{jk}\mathcal{S}_{\Gamma_{jk}}(u_k^{\{h,n-1\}}), \mathcal{S}_{\Gamma_{jk}}(v)\right\rangle_{\Gamma_{jk}}$$

$$+ \sum_k \left\langle\left\langle \lambda_{kj}^{\{h,n-1\}}, \mathcal{S}_{\Gamma_{jk}}(v)\right\rangle\right\rangle_{\Gamma_{jk}}, \quad v \in \mathcal{N}C^h(\Omega_j) \times \mathcal{W}_j^h,$$

$$\lambda_{jk}^{\{h,n\}} = \lambda_{kj}^{\{h,n-1\}} - i\omega\beta_{jk}[S_{\Gamma_{jk}}(u_j^{\{h,n\}} + S_{\Gamma_{kj}}(u_k^{\{h,n-1\}})](\xi_{jk}), \quad \text{on } \Gamma_{jk}, \forall k. \tag{10b}$$

Equation (10b), used to update the Lagrange multipliers, is obtained directly from (8b) evaluated at the mid point $\xi_{jk}$.

Equation (10a) yields a $12 \times 12$ linear system of equations for the degrees of freedom associated with the vector displacements of the solid and fluid phases on each subdomain $\Omega_j$ at the $n-$iteration level. The iteration (10a)–(10b) is a Jacobi–type iteration. A twice as fast iteration may also be defined by using a **red–black** type iteration ( see (J. Douglas Jr. et al., 2001; Ha et al., 2002; Santos and Sheen, 2006)). The iteration parameter matrix $\beta_{jk}$ is chosen to have the same form of the matrix $\mathcal{D}$ in (6), with entries obtained by averaging the coefficients in the definition of the matrices $\mathcal{A}$ and $\mathcal{M}$ in (7) on both sides of the boundary $\Gamma_{jk}$.

The space–time solution is obtained by solving (10) for a finite number of temporal frequencies and using an approximate inverse Fourier transform (J. Douglas Jr. et al., 1993).

## 4 NUMERICAL EXPERIMENTS

We consider wave propagation in a poroelastic medium $\Omega$ of uniform porosity $\phi = 0.3$ and permeability $k = 1$ Darcy, saturated with either gas or water. The value of the structure factor $S$ in (2) was chosen to be 1. The other material properties of the system are given in Table 1.

| Solid Matrix | solid grains bulk modulus, $K_s$ | 37 GPa |
|---|---|---|
| | dry matrix bulk modulus, $K_m$ | 8 GPa |
| | dry matrix shear modulus, $\mu$ | 9.5 GPa |
| | solid grains density, $\rho_s$ | 2650 kg/m$^3$ |
| Water | bulk modulus, $K_f$ | 2.25 GPa |
| | density, $\rho_f$ | 1040 kg/m$^3$ |
| | viscosity, $\eta$ | 3 cP |
| Gas | bulk modulus, $K_f$ | 0.012 GPa |
| | density, $\rho_2$ | 78 kg/m$^3$ |
| | viscosity, $\eta$ | 0.15 cP |

Table 1. Material properties of the system

The domain $\Omega$ is a rectangle with horizontal side length $L_x = 360$ m and vertical side length $L_y = 720$ m. The domain $\Omega$ is divided into two regions

$$\Omega_{homo} = \{0 < x < 360\,\text{m}, \quad 0 < y < 8.8\,\text{m}\}, \qquad \Omega_{per} = \{0 \leq x < 360\,\text{m}, \quad 8.8 < y < 720\,\text{m}\}.$$

The region $\Omega_{homo}$ is fully saturated with water, while the region $\Omega_{per}$ consists of horizontal layers of width 40 cm alternatively saturated with either gas or water. In order to analyze the mesoscopic loss mechanism it is convenient first to approximate the saturated porous medium $\Omega$ by a viscoelastic solid and use the concept of complex velocity as follows. Recall that in a viscoelastic solid, the quality factor $Q(\omega)$ is defined by the relation

$$Q(\omega) = \frac{\text{Re}(v_p^2)}{\text{Im}(v_p^2)},$$

where $v_p$ is the complex compressional velocity given by

$$v_p(\omega) = \sqrt{\frac{E}{\overline{\rho}_b}}. \qquad (11)$$

In (11) $\overline{\rho}_b$ is the average bulk density over $\Omega$ and $E = E(\omega) = |E|e^{i\theta}$ is the complex plane wave modulus associated with the domain $\Omega$ as defined by White (White et al., 1975), which complicated expression involving all coefficients in Biot's equations of motion (3) is not included here for brevity. The quality factor is related to the loss angle $\theta$ by the formula

$$Q^{-1}(\omega) = \tan\theta.$$

Figure 2 displays the inverse of the quality factor $Q(\omega)$, showing that the minimum value of $Q(\omega)$ is approximately equal to 28 corresponding to a frequency of 20 Hz. This frequency was chosen as the dominant frequency of the external source to be used in our numerical simulations, which allowed us to better visualize the attenuation effects being analyzed.

Figure 3 shows the phase velocity $c_p(\omega)$ obtained from the expression

$$c_p(\omega) = \left[\text{Re}\left(\frac{1}{v_p(\omega)}\right)\right]^{-1},$$

where it can be observed the velocity dispersion associated with the wave-induced fluid flow mechanism.

The source function $(F^s, F^f)$ is a compressional point source located inside the region $\Omega_{homo}$ at $(x_s, y_s) = (180 \text{ m}, 4 \text{ m})$ applied to the solid frame given by

$$F^s(x, y, \omega) = \nabla\delta_{x_s,y_s}\ g(\omega), \qquad , F^f = 0,$$

where $\delta_{x_s,y_s}$ denotes the Dirac distribution at $(x_s, y_s)$. Also, $g(\omega)$ is the Fourier transform of the waveform

$$g(t) = -2\xi(t - t_0)e^{-\xi(t-t_0)^2},$$

with $\xi = 8\ f_0^2$, $t_0 = 1.25/f_0$, where the value $f_0$ was chosen such that the source central (dominant) frequency be equal to 20 Hz.

The parallel iterative procedure (10a)- (10b) was used to find the time Fourier transforms of the displacement vectors of the solid and fluid phases for 110 equally spaced temporal frequencies in the interval $(0, 60\text{Hz})$ employing a uniform partition $\mathcal{T}^h$ of $\Omega$ into squares of side length $h = 40$ cm. The time domain solution was obtained after performing an approximate inverse Fourier transform. The numerical experiments were run in the IBM SP2 and the Community Cluster parallel computers at Purdue University under the MPI standard.
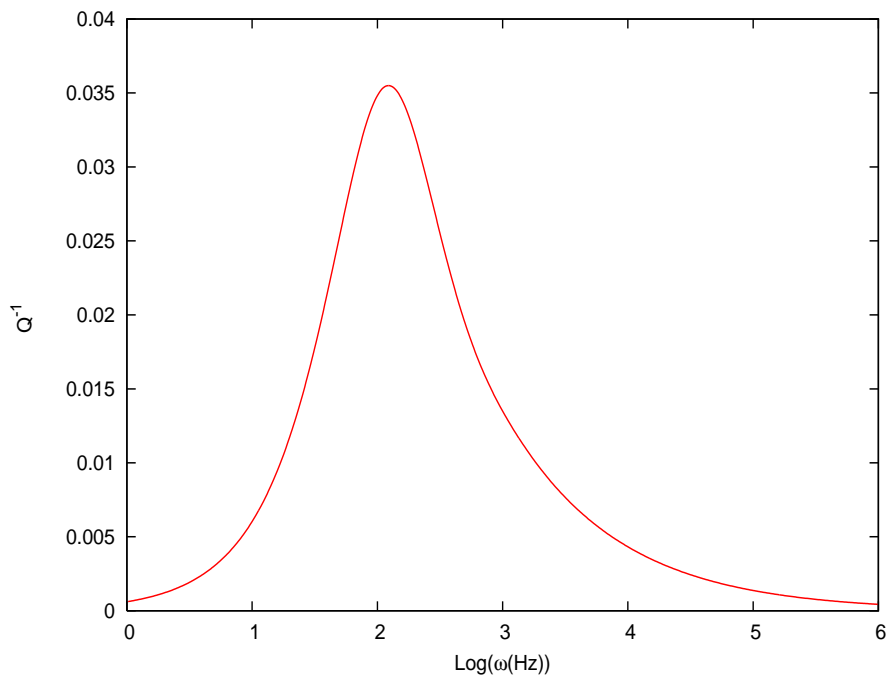
Figure 2: Inverse of quality factor for a sandstone saturated with water and gas
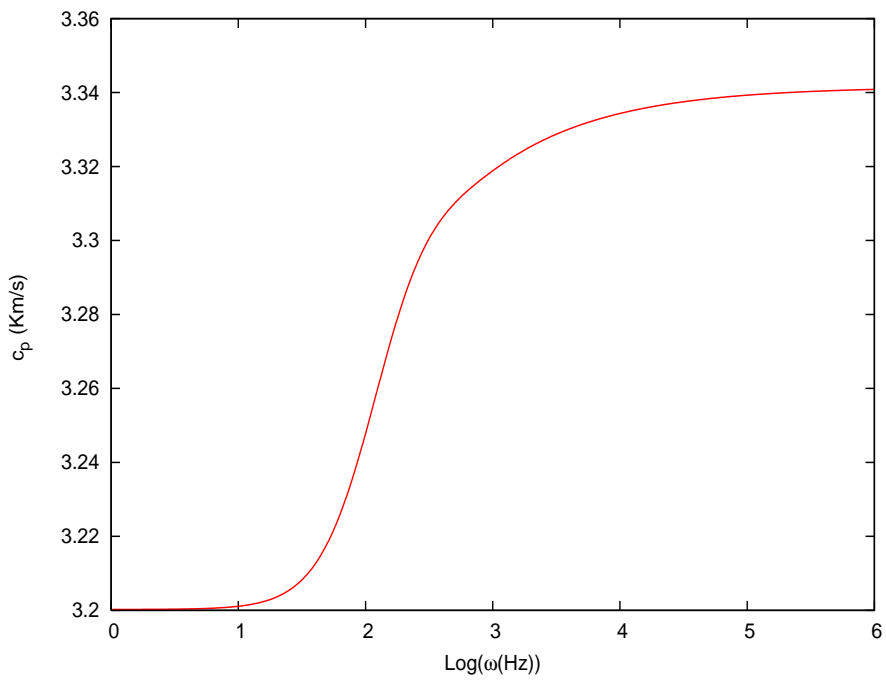


Figure 3: Phase velocity for a sandstone saturated with water and gas

To observe the mesoscopic attenuation effects we also run the same experiment but when the domain $\Omega$ is fully saturated with either water or gas.

Figures 4, 5 and 6 show traces of the vertical component of the particle velocity of the solid phase for the three cases studied, *i.e.*, the periodic gas-water saturated case, and the homogeneous water and gas saturated cases at three receivers $r_j$ with receiver locations $(x_{rj}, y_{rj}), j = 1, 2, 3$, where $x_{rj} = 180$ m, $j = 1, 2, 3$ and $y_{r1} = 230$ m, $y_{r2} = 456$ m, $y_{r3} = 682$ m.

The amplitude peaks corresponding to the arrival of the fast P1 wave of the traces in the case of periodic gas-water saturation are lower than the corresponding peaks for the cases of homogeneous water saturation in Figure 5 and of homogeneous gas saturation in Figure 6, showing clearly the mesoscopic loss mechanism predicted by White (White et al., 1975). This effect is more easily observed in Figure 7 where traces of the vertical component of the particle velocity of the solid phase at the receiver $r_3$ are shown for the three cases analyzed. Note also the delay in the arrival time of the pulse for the periodic gas-water case as compared with the homogeneous water and gas cases, showing the velocity dispersion effects caused by the mesoscopic-scale heterogeneities.

Notice that the decay rate of the peaks associated with the arrival of the fast P1 wave in Figure 4 is much larger than the corresponding decay rates in Figures 5 and 6, which are associated only with the geometrical spreading effects. The fast decay rate of the peak amplitudes in Figure 4 is then caused by the wave-induced flow between the gas and water layers.

The quality factor $Q(\omega)$ associated with this decay rate can be evaluated by using the frequency shift method analyzed by Quan et. al (Quan and Harris, 1997). Here we briefly describe the procedure.

Let $A(f, r_s)$ be the value of the amplitude spectrum of the trace of the vertical component of the displacement of the solid phase observed at the receiver $r_s$ located at a distance $d_s$ from the source at the frequency $f = \omega/2\pi$. Let $f_s$ be the centroid of $A(f, r_s)$, defined by the formula

$$f_s = \frac{\int_o^\infty f A(f, r_s) df}{\int_o^\infty A(f, r_s) df}.$$

The frequency shift method relates the quality factor Q with the centroid frequencies $f_s$ and $f_t$ of two receivers $r_s$ and $r_t$, respectively, considering the signal at the receiver $r_s$ as the source for the receiver $r_t$. For the special case when the amplitude spectrum of the signal $A(f, r_s)$ at the receiver $r_s$ is Gaussian with variance $\sigma_s^2$, the following equality holds (Quan and Harris, 1997)

$$\frac{\pi(d_t - d_s)}{Q c_p} = (f_s - f_t)/\sigma_s^2, \tag{12}$$

where $c_p$ is the average compressional phase velocity in a region containing the receivers $r_s$ and $r_t$ in the frequency band of interest $(0, 60\text{Hz})$. The value of $c_p$ was estimated from the arrival times at the corresponding receivers.

For the receiver pairs $(r_1, r_2)$, $(r_2, r_3)$ and $(r_1, r_3)$, (12) yields the estimates $Q_{12} = 29.96$, $Q_{23} = 24.63$ and $Q_{13} = 28$. These values are in very good agreement with the theoretical value ($Q = 28$ at 20 Hz) of the quality factor predicted by White (White et al., 1975) as shown in Figure 2.

## 5    CONCLUSIONS

For a medium consisting of alternating porous layers saturated with gas and water, the numerical experiments have shown that the mesoscopic loss mechanism can affect the observed
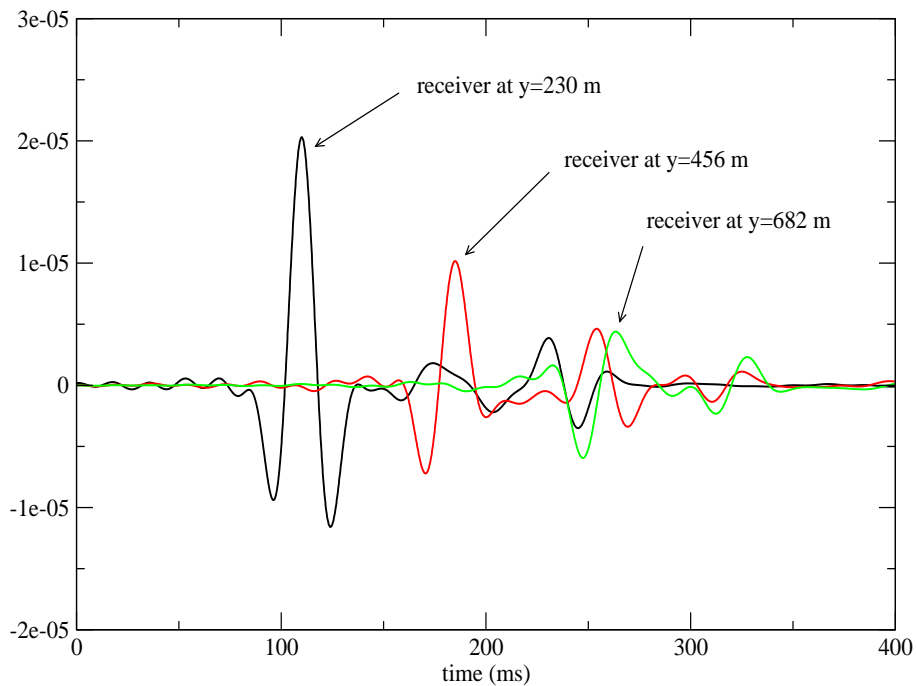
Figure 4: Traces of the vertical component of the particle velocity of the solid phase in a periodic gas-water saturated porous medium

traces in the seismic band, confirming the predictions in (White et al., 1975). This is a simple example of how microheterogeneities in the fluid and frame properties can affect observations at the macroscale. The numerical experiments show that the finite element procedure employed is accurately representing the attenuation effects, and could be employed to analyze this phenomenon in highly heterogeneous porous materials, such as in the case of patchy saturation or fractal porosity-permeability distributions.
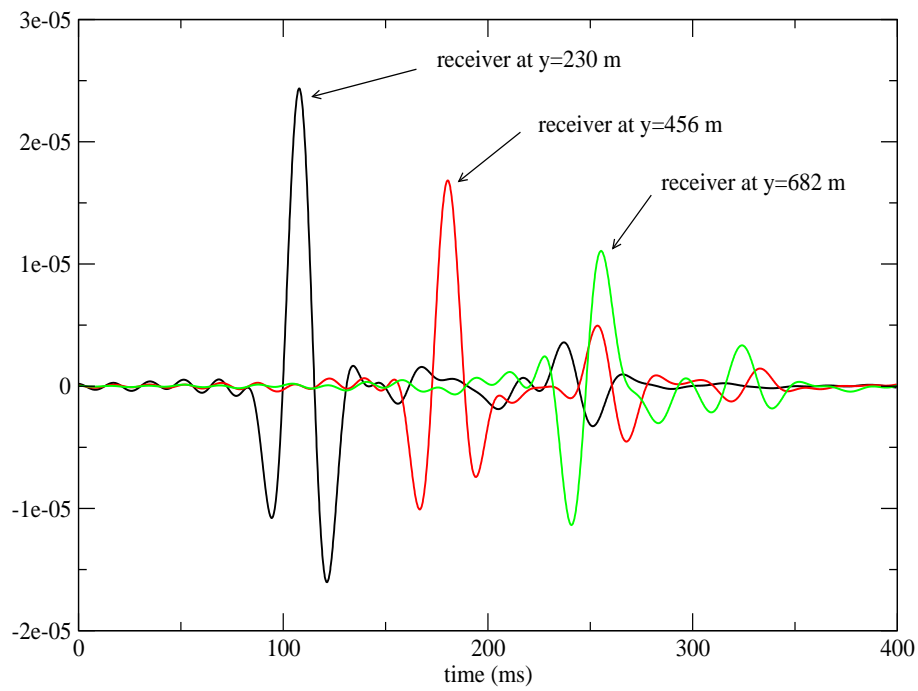
## 6   AKNOWLEDGEMENTS

Figure 5: Traces of the vertical component of the particle velocity of the solid phase in a water-saturated porous medium
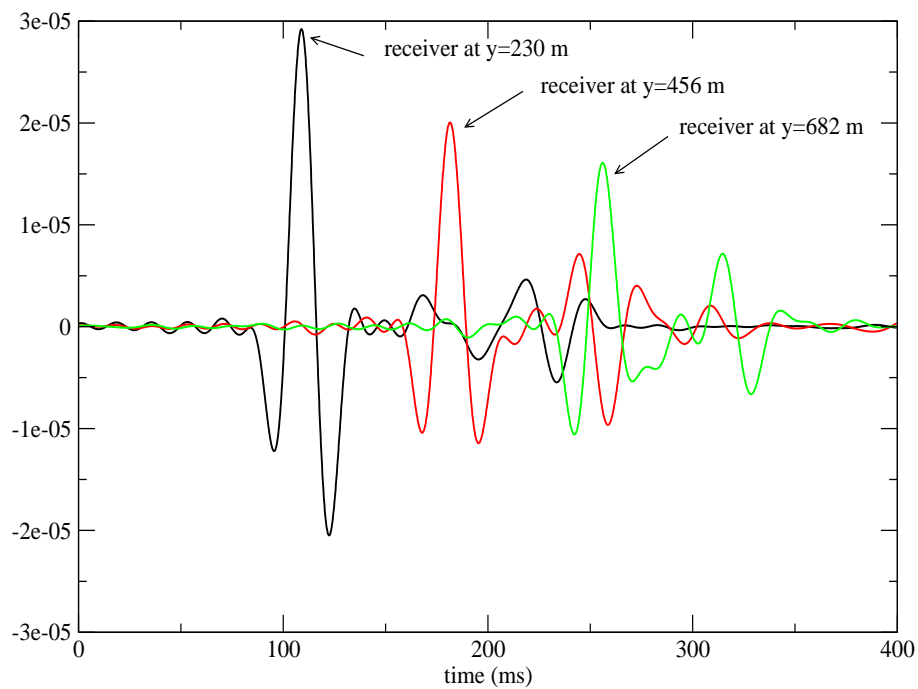


Figure 6: Traces of the vertical component of the particle velocity of the solid phase in a gas-saturated porous medium
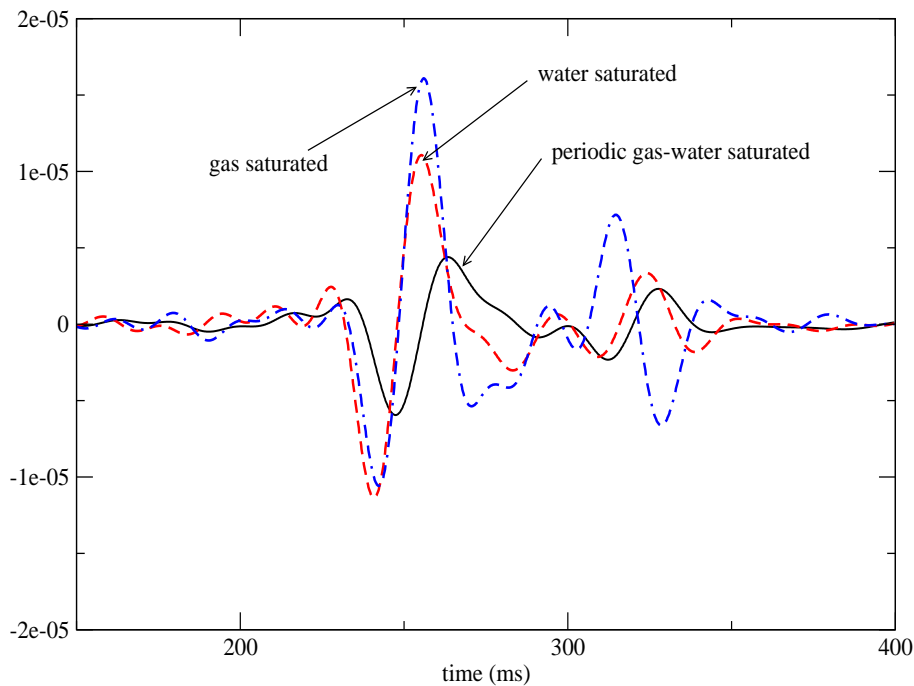
Figure 7: Traces of the vertical component of the particle velocity of the solid phase at receiver $r_3$ located at $x = 180$ m, $y = 682$ m for a periodic gas-water, water and gas saturated porous medium, respectively

## REFERENCES

M. A. Biot. Theory of propagation of elastic waves in a fluid-saturated porous solid. I. Low frequency range. *J. Acoust. Soc. Am.*, 28:168–171, 1956a.

M. A. Biot. Theory of propagation of elastic waves in a fluid-saturated porous solid. II. High frequency range. *J. Acoust. Soc. Am.*, 28:179–191, 1956b.

M. A. Biot. Mechanics of deformation and acoustic propagation in porous media. *J. Appl. Phys.*, 33:1482–1498, 1962.

J. M. Carcione, H. B. Helle, and N. H. Pham. White's model for wave propagation in partially saturated rocks: Comparison with poroelastic numerical experiments. *Geophysics*, 68:1389–1398, 2003.

F. Gassmann. über die elastizität poröser medien" ("on the elasticity of porous media"). *Vierteljahrsschrift der Naturforschenden Gessellschaft in Zurich*, pages 1–23, 1951.

T. Ha, J. E. Santos, and D. Sheen. Nonconforming fi nite element methods for the simulation of waves in viscoelastic solids. *Computer Methods in Appl. Mech. and Eng.*, 191:5647–5670, 2002.

H. B. Helle, N. H. Pham, and J. M. Carcione. Velocity and attenuation in partially saturated rocks. poroelastic numerical experiments. *Geophysical Prospecting*, 51:551–566, 2003.

J. Douglas Jr., J. E. Santos, and D. Sheen. Nonconforming galerkin methods for the helmholtz equation. *Numer. Methods for Partial Diff. Equations*, 17:475–494, 2001.

J. Douglas Jr., J. E. Santos, D. Sheen, and L. Bennethum. Frequency domain treatment of one–dimensional scalar waves. *Math. Models Methods Appl. Sci.*, 3:171–194, 1993.

J. Douglas Jr., J. E. Santos, D. Sheen, and X. Ye. Nonconforming Galerkin methods based on quadrilateral elements for second order elliptic problems. *RAIRO Math. Modeling and Numer. Analysis (M2AN)*, 33:747–770, 1999.

J. C. Nedelec. Mixed fi nite elements in $r^3$. *Numer. Math.*, 35:315–341, 1980.

Y. Quan and J. M. Harris. Seismic attenuation tomography using the frequency shift method. *Geophysics*, 62:895–905, 1997.

P. A. Raviart and J. M. Thomas. Mixed finite element method for $2^{nd}$ order elliptic problems. *Mathematical Aspects of the Finite Element Methods, Lecture Notes of Mathematics, vol. 606, Springer*, 1975.

J. E. Santos, J. M. Corberó, C. L. Ravazzoli, and J. L. Hensley. Reflection and transmission coefficients in fluid-saturated porous media. *J. Acoust. Soc. Amer.*, 91:1911–1923, 1992.

J. E. Santos and D. Sheen. Finite element methods for the simulation of waves in composite saturated poroviscoelastic media. *Siam J. Numer. Anal., to appear*, 2006.

J. E. White, N. G. Mikhaylova, and F. M. Lyakhovitskiy. Low-frequency seismic waves in fluid-saturated layered rocks. *Izvestija Academy of Siences USSR, Physics of Solid Earth*, 10: 654–659, 1975.

F. I. Zyserman, P. M. Gauzellino, and J. E. Santos. Dispersion analysis of a non-conforming finite element method for the helmholtz and elastodynamic equations. *Int. J. Numer. Meth. Eng.*, 58:1381–1395, 2003.